Synthesis of N-TiO$_2$/BiOI/RGO composites with significantly enhanced visible light photocatalytic activity

Limei Xue[1,a)], **Fengzhi An**[1,b)], **Yanhao Yang**[2], **Yuan Ma**[3]

[1]*School of Environment and Chemical Engineering, Heilongjiang University of Science & Technology, Harbin 150022, China*
[2]*Suzhou Lai School Education Technology Co. Ltd., Jiangsu, Suzhou 215000, China*
[3]*State Grid Xinyuan Compant Ltd., Jilin, Dunhua 133700, China*
[a)]Address all correspondence to these authors. e-mail: 547417039@qq.com
[b)]e-mail: 1415222469@qq.com
Contributing Editor: Limei Xue

In this work, four N-TiO$_2$/bismuth oxyiodide (BiOI)/reduced graphene oxide (RGO) composite photocatalysts with different composite ratios were prepared using a hydrothermal method. The phase, surface structure, specific surface area, and light response were characterized by X-ray diffraction, X-ray photoelectron spectrum analysis, scanning electron microscopy, specific surface area and aperture analysis, and UV-vis diffuse reflection spectrum analysis. The results indicated that the N-TiO$_2$/BiOI/RGO (NTGB) composite prepared with a mass ratio of 1:1:2 is a promising photocatalyst for the degradation of organic pollutants by using sunlight, with a specific surface area of 139.56 (m^2/g), bandgap of 1.24 eV, and strong absorption with a smaller visible region.

It has the best photocatalytic properties under visible light irradiation in the degradation of methylene blue (MB): the degradation rate of MB in the presence of light for 60 min reached 99.22%, and its photocatalytic performance was significantly higher than that of TiO$_2$, N-TiO$_2$, BiOI, N-TiO$_2$/BiOI, BiOI/RGO, NTGB1, NTGB2, and NTGB4.

Introduction

As environmental problems become more and more serious, it is important to find an efficient and eco-friendly way to govern the environment. Photocatalytic technology has attracted considerable attention from both academia and industry because it uses solar energy to degrade air and water pollutants with high efficiency and without causing pollution [1, 2, 3, 4]. Titanium dioxide (TiO$_2$) is a kind of n-type semiconductor photocatalyst, and has received wide research interests owing to its advantages of non-toxic, cheap and stable physical and chemical properties. However, because of the large bandgap (about 3.2 eV) of TiO$_2$, it can only be excited by ultraviolet light (represents 3–5% of the total sunlight energy), which limits its wide application [5, 6, 7, 8, 9]. To improve the efficiency of solar energy utilization, researchers have been working on photocatalytic materials that have the capability to respond to visible light (represents 43% of the total solar energy). Doping TiO$_2$ with nonmetallic elements [10, 11, 12, 13] can form sublayers, reduce the bandgap width of TiO$_2$, form traps in

TiO$_2$, reduce the recombination rate of photogenerated excitons (electron–hole pairs), and improve the photocatalytic activity. Fabricating a TiO$_2$-based heterojunction structure using a narrow-bandgap semiconductor with band potentials that match those of TiO$_2$ allows the photogenerated carriers from the narrow-bandgap semiconductor to be transferred to TiO$_2$ via the heterojunction interface. Such charge transfer contributes to the efficient charge separation, such as in NiO/TiO$_2$ [14], Ag$_2$O/TiO$_2$ [15], Bi$_2$S$_3$/TiO$_2$ [16], and CdS/TiO$_2$ [17].

Bismuth oxyiodide (BiOI) is a p-type semiconductor photocatalyst [18]. BiOI has a bandgap of 1.75 eV [19] and, therefore, can be directly used as a visible light catalyst. However, due to its narrow bandgap, the photogenerated exciton migration path is too short, resulting in a high recombination rate and poor photocatalytic performance. Studies have shown that TiO$_2$/BiOI heterojunction photocatalysts can promote the separation of photogenerated excitons to free electrons and holes, thus improving the photocatalytic performance under visible light [20]. However, TiO$_2$/BiOI

photocatalysts still have the disadvantages of low specific surface area and insufficient visible light absorption. Graphene (GR) or reduced graphene oxide (RGO) is known as one of the materials with the fastest electron transfer rate, high electrical conductivity, good chemical stability, and a large specific surface area. Therefore, GR or RGO can timely transfer electrons, thus inhibiting charge recombination. Previous studies have shown that RGO ternary composite photocatalysts (e.g., Ag/TiO$_2$/RGO [21], RGO/Ag/Cu$_2$O [22], and Sn$_3$O$_4$/SnO$_2$/RGO [23]) possess stable light absorption capability under visible light irradiation and good visible light catalytic activity.

In this work, a nitrogen-doped titanium dioxide (N-TiO$_2$)/BiOI/RGO heterostructure composite was synthesized by using a hydrothermal method. The photocatalytic property of the N-TiO$_2$/BiOI/RGO (NTGB) composite was evaluated by investigating the degradation of methylene blue (MB) under visible light irradiation. The results indicated that the NTGB heterostructure composite had excellent performance toward the degradation of MB under visible light irradiation.

Results and discussion

Crystal structure and morphology characterization of samples

Figure 1(a) shows the X-ray diffraction (XRD) patterns of as-prepared graphene oxide (GO), TiO$_2$, N-TiO$_2$(NT), BiOI, and NTGB3 (mass ratio of NT:BiOI:RGO = 1:1:2). The XRD peak at 10.2° corresponds to the (001) reflection in graphene oxide. The characteristic peak of the GO (101) crystal plane

disappeared in NTGB3, indicating that the hydrothermal reaction reduced GO to RGO. It can be seen that the diffraction peaks of the XRD patterns are in agreement with the standard values of TiO$_2$ with a tetragonal anatase phase (JCPDS card No. 21-1272) and BiOI with a tetragonal structure (JCPDS card No. 73-2062), respectively. For the sample of NTGB3, the characteristic peaks appeared at 25.5°, 38.1°, 48.2°, and 54.6° and are assigned to the (101), (004), (200), and (105) lattice planes, respectively, whereas for the sample of BiOI, the main diffraction peak positions were located at 29.7°, 31.7°, 39.4°, 45.6°, 51.5°, 55.2°, and 66.2° and are assigned to (012), (110), (013), (020), (114), (122), and (220), respectively. As can be seen from the inset in Fig. 1(a), the diffraction peak positions corresponding to the (101) crystal planes of NTGB3 and NT were significantly shifted to smaller 2θ compared with TiO$_2$. It is indicated that N-doping leads to the distortion of TiO$_2$ lattice, which might originate from the coexistence of the substitution position (N-Ti–O) and gap position (N-O–Ti) in N-doped TiO$_2$ [24].

Fig. 1(b) shows the XRD patterns of NTGB ternary composites synthesized by varying the weight ratios of the components. The crystallite size of the NTGB present in the system was calculated using the Debye–Scherrer formula:

$$d = K/\beta \cos \theta \qquad (1)$$

where d is the crystallite size, K is the dimensionless shape factor (here taken to be 0.94), λ is the wavelength of the X-ray used, and β is the full width at half maximum corresponding to the Bragg angle θ. Based on XRD, the grain sizes were calculated to be 23.21, 11.81, 7.70, and 8.30 nm for NTGB1
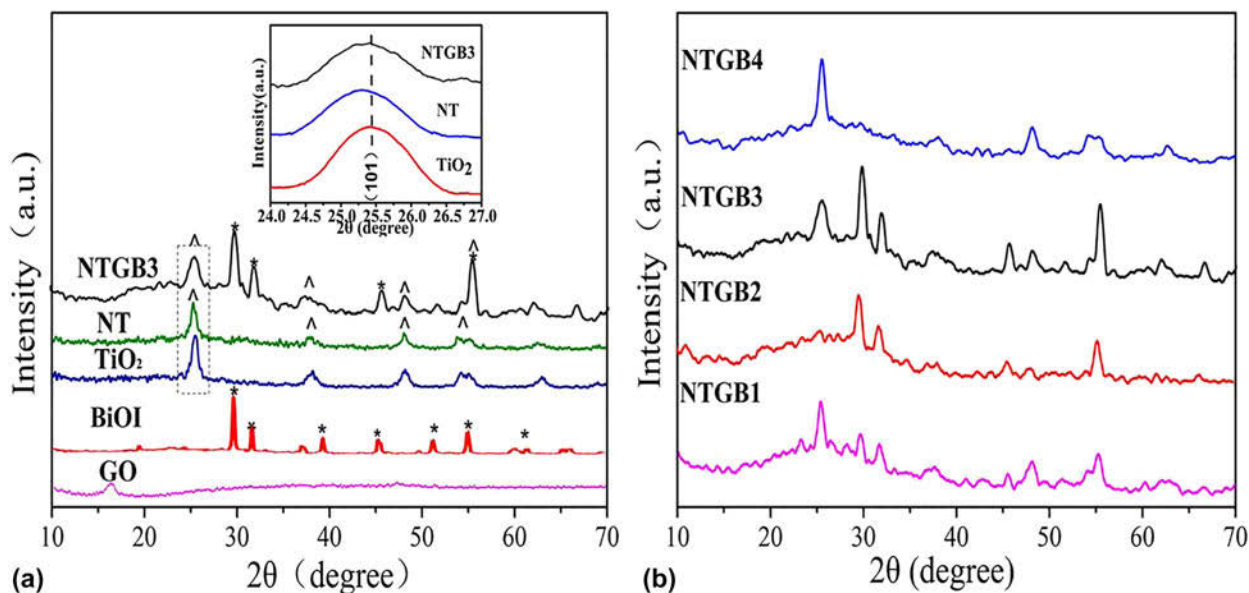

Figure 1: (a) XRD patterns of GO, TiO$_2$, NT, BiOI, and NTGB3 illustrated with the (101) crystal plane of TiO$_2$, NT, and NTGB3 (* is BiOI; ^ is NT), (b) XRD pattern of NTGB components.
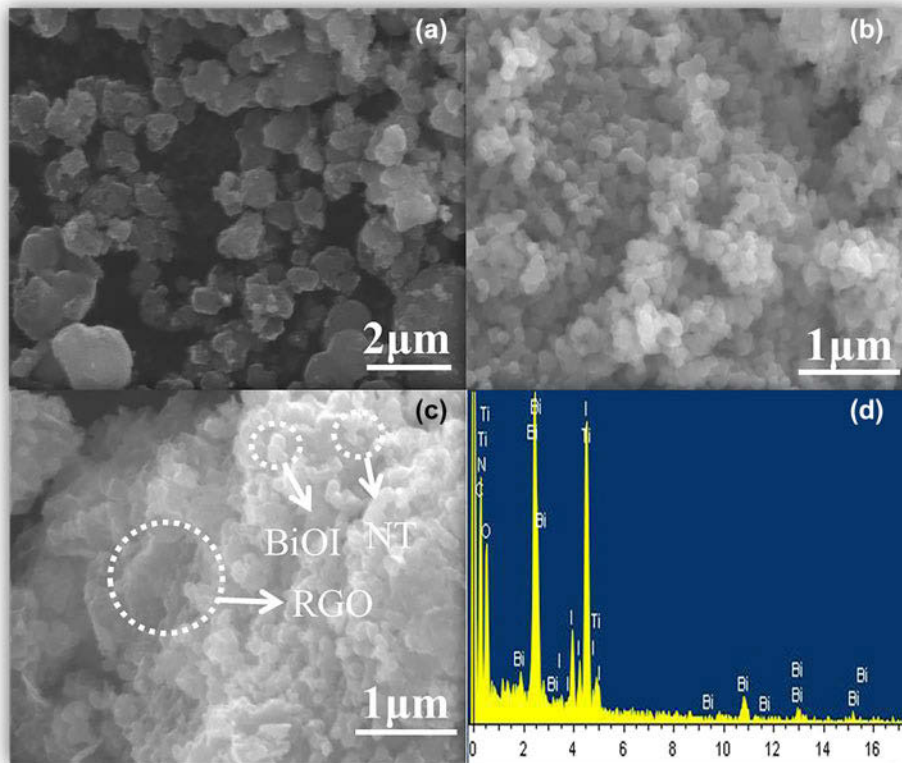
Figure 2: SEM images of (a) NT, (b) BiOI, and (c) NTGB3; (d) EDS of NTGB3.

(mass ratio of NT:BiOI:RGO = 1:1:1), NTGB2 (mass ratio of NT:BiOI:RGO = 1:2:1), NTGB3, and NTGB4 (mass ratio of NT:BiOI:RGO = 2:1:1), respectively.

In order to further study the morphology and microstructure, scanning electron microscopy (SEM) and energy dispersive spectroscopy (EDS) of NTGB3 were also observed. As shown in Fig. 2(a), NT powder particles are random-shaped, and BiOI [Fig. 2(b)] is a loose aggregate formed by a large number of small particles. As shown in Fig. 2(c), NT and BiOI are attached to the surface of RGO. Figure 2(d) shows the EDS spectrum of NTGB3. The EDS measurement further reveals the main signals of the photocatalyst's main elements (C, Ti, N, O, Bi, and I).

Structural and compositional characterization

The X-ray photo-electron spectroscopy (XPS) spectra of the NTGB3 composite are further studied in order to explore the chemical composition and oxidation state of the as-prepared samples. Fig. 3(a) shows the peaks of Ti, O, N, Bi, I, and C. The high-resolution peaks of the elements were further fitted. In the Ti $2p$ spectrum [Fig. 3(b)], two peaks are located at 458.5 and 464.4 eV, corresponding to the Ti $2p_{3/2}$ and Ti $2p_{1/2}$ of Ti^{+4}. Figure 3(c) shows the XPS spectrum of O $1s$. The electron binding energies are 529.8 and 530.5 eV, which are attributed

to Ti–O in TiO$_2$ and Bi–O in BiOI, respectively. The characteristic peak of 531.8 eV is attributed to the O–H bond which originated from the surface absorbed water. The peak of 532.5 eV is attributed to the C=O and C(O)O bonds [25]. The XPS spectra of N $1s$ are presented in Fig. 3(d); the peak of 398.4 eV in the sample corresponds to the binding energy of N $1s$, and the N element may enter the TiO$_2$ lattice by gap doping. In Fig. 3(e), two strong peaks located at about 159.4 and 164.8 eV are assigned to Bi $4f_{5/2}$ and Bi $4f_{7/2}$, suggesting that the existence of the Bi element is Bi^{3+} [26]. The spectrum of I $3d$ in Fig. 3(f) displays two peaks at about 619.2 and 630.7 eV, corresponding to I $3d_{5/2}$ and I $3d_{3/2}$ of I$^-$, respectively. The peaks at 284.5, 285.7, and 288.5 eV in Fig. 3(g) are attributed to the C=C bond, C–O bond, and C(O)O bond [27], respectively. The strong C=C peak indicates that GO is reduced to RGO through the hydrothermal reaction and compounded with NT and BiOI.

Figure 4 shows the isotherms and pore size distribution curves of pure NTGB3 samples. It can be seen from Fig. 4 that the N$_2$ adsorption–desorption isotherms of NTGB3 exhibit the classical type IV curves with an H1 adsorption hysteresis loop according to the International Union of Pure and Applied Chemistry (IUPAC) classification. The NTGB3 composite has a narrow range of uniform mesopores. In addition, it can be
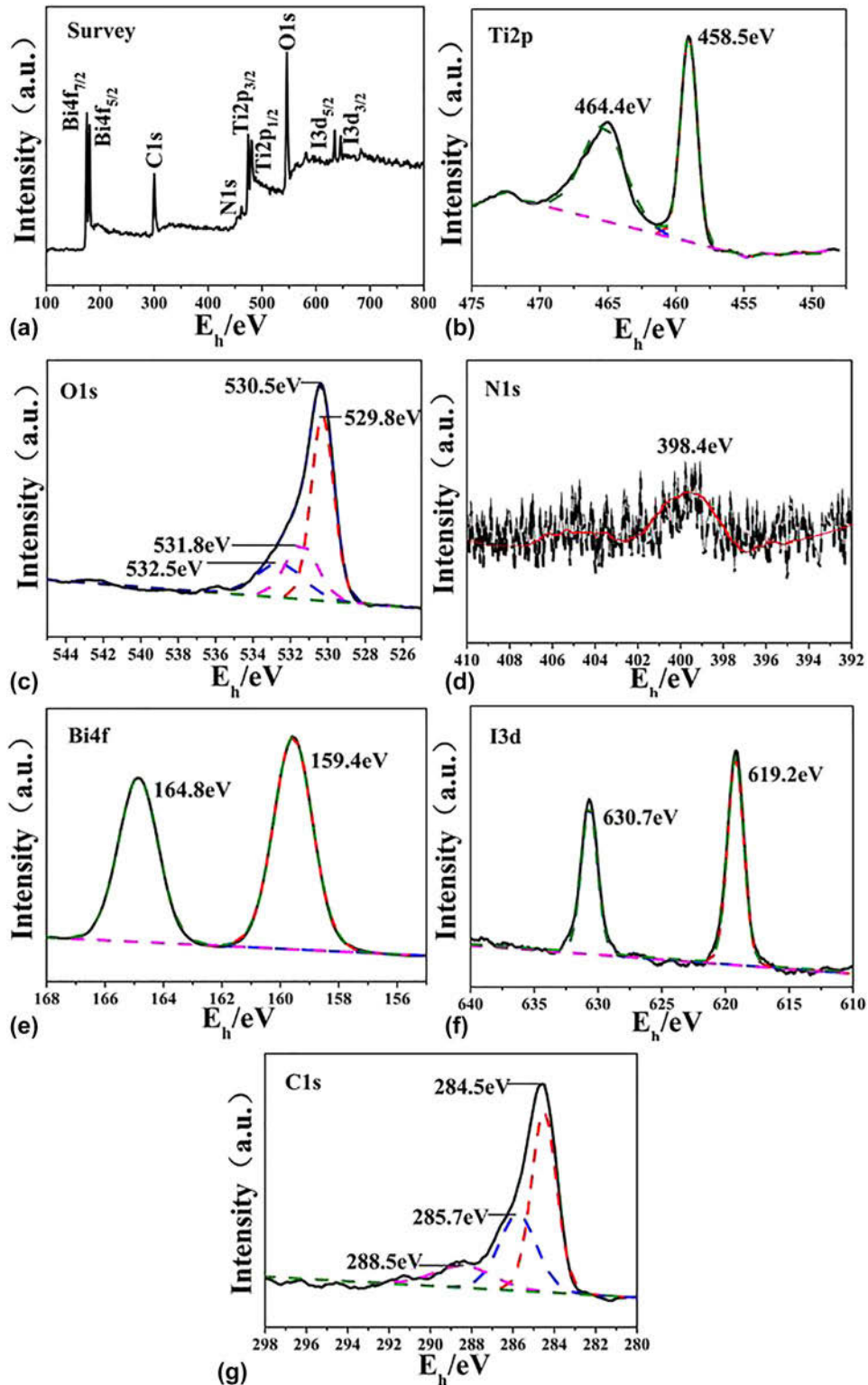
Figure 3: XPS spectra of the NTGB3 composite: (a) full scan survey of NTGB3, (b) Ti 2*p*, (c) O 1*s*, (d) N 1*s*, (e) Bi 4*f*, (f) I 3*d*, and (g) C 1*s*.

seen from Table I that the specific surface area (S_{BET}) of TiO$_2$ is 85.37 m^2/g. Due to the doping of the N element, the S_{BET} of NT increases by 8.11 m^2/g compared with that of TiO$_2$, while the S_{BET} of BiOI is 3.35 m^2/g. Due to the small S_{BET} of BiOI, the

S_{BET} of the NTB composite is smaller than that of TiO$_2$. The NTGB3 composite has the largest S_{BET} due to the contribution of RGO's large specific surface area. The higher specific surface area of the NTGB3 composite is conducive to the adsorption of
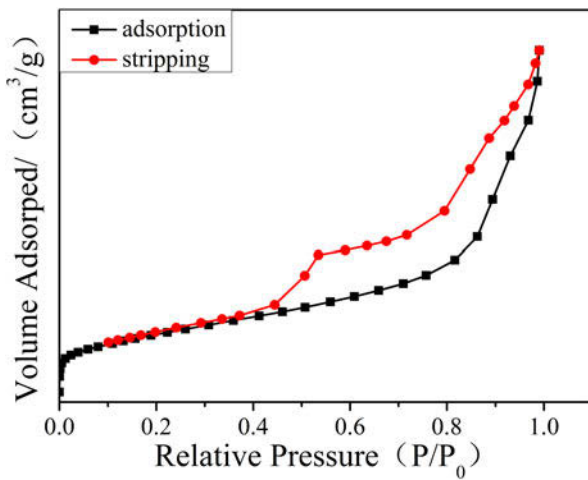
Figure 4: Adsorption and desorption isotherms of NTGB3.

TABLE I: Specific surface areas of each sample.

Samples	TiO$_2$	NT	BiOI	NTB	NTGB1	NTGB2	NTGB3	NTGB4
S_{BET} (m^2/g)	85.37	93.48	3.35	63.90	99.23	93.78	139.56	110.73

feed reactants and the subsequent photocatalytic reaction on the surface. The increased specific surface area can absorb more light intensity and generate more excitons, which is conducive to the degradation of MB in the photocatalytic process [28].

Optical absorption property analysis

Light absorption is an important parameter of semiconductors from which the corresponding bandgap of materials can be calculated. Figure 5 displays the UV-vis diffuse reflection spectrum (UV-vis DRS) of the TiO$_2$, NT, BiOI, RGO, N-TiO$_2$/BiOI (NTB), BiOI/RGO (BG), and NTGB3 photocatalysts. As shown in Fig. 5(a), TiO$_2$ has weak absorption in the visible region of lambda >400 nm. A slight "redshift" absorption was observed for the n-doped NT absorption, possibly because hybridization of the 2p state of nitrogen with the 2p state of oxygen reduces the bandgap [29]. BiOI has a strong absorption in the visible region of 400–650 nm. The BiOI/NT composite has a strong absorption in the visible region of 400–650 nm, and the absorption edge is about 650 nm. This indicates that BiOI can effectively broaden the absorption of NT, improve the photonic quantum efficiency of NT in the visible region, and accelerate the formation rate of photogenerated electron–hole pairs. The combination of BiOI and NT produces a good synergy and reduces the bandgap. BG has a strong absorption in the visible region of 400–650 nm and weak absorption in the range of 650–1100 nm. The photocatalyst of NTGB3 combined with BiOI and NT has strong absorption at 380–1100 nm. Compared with NTB, its optical

response range is wider and the optical absorption intensity is higher. RGO plays an important role in broadening the optical response range in the resulting composites. Figure 5(b) shows the plots of $(ah\nu)^{1/2}$ versus photo energy ($h\nu$) for TiO$_2$, NT, BiOI, RGO, NTB, BG, and NTGB3. According to the results of optical absorption properties, the bandgap energy (E_g) of the samples can be determined by the following equation:

$$(ah\nu)^{1/2} = A(h\nu - E_g) \qquad (2)$$

where a is the optical absorption coefficient, $h\nu$ is the photonic energy, A is a constant, and E_g is the bandgap energy. As shown in Fig. 5(b), TiO$_2$, NT, BiOI, RGO, NTB, BG, and NTGB3 have bandgaps of 3.23, 3.16, 1.75, 0, 1.68, 1.65, and 1.24 eV, respectively. NTGB3 has a relatively narrow bandgap.

Figure 6 displays the UV-vis DRS of NTGB photocatalysts with different mass composition ratios. As shown in Fig. 6(a), NTGB with different recombination ratios showed different light absorption intensities. Among them, NTGB3 shows superior visible light absorption. Figure 6(b) shows the plots of $(ah\nu)^{1/2}$ versus the photo energy ($h\nu$) for NTGB with different mass composition ratios. As shown in Fig. 6(b), the bandgaps of NTGB1, NTGB2, NTGB3, and NTGB4 are 1.39, 1.32, 1.24, and 2.4 eV, respectively.

Photocatalytic properties

The photocatalytic performance of NTGB was evaluated by the visible light degradation effect of MB. Figure 7 shows the absorption spectra of the MB solution photocatalyzed by NTGB3 for different times. As the photocatalytic degradation progresses, the absorption peak intensity of MB at 664 and 292 nm gradually decreases. Figure 8 shows the photocatalytic degradation curves of the MB solution by different catalysts. It can be seen that MB does not degrade under the condition of no light and no catalyst, indicating that the photocatalytic reaction does not occur. When TiO$_2$, NT, NTB, BG, BiOI, NTGB1, NTGB2, NTGB3, and NTGB4 photocatalysts are used and subjected to the presence of light for 60 min, MB shows different degradation degrees. The degradation rate of NTGB3 to MB was 99.22%, which was 1.39, 1.32, 1.31, 1.30, 1.28, 1.05, 1.09, and 1.13 times higher than that of TiO$_2$, NT, BiOI, NTB, BG, NTGB1, NTGB2, and NTGB4, respectively. At the same time, the transport and separation efficiency of TiO$_2$ and BiOI photoelectron–hole pairs are improved, and the exciton recombination of TiO$_2$ and BiOI is inhibited, thereby improving the photocatalytic activity. In addition, NTGB3 has a narrow bandgap and excellent light absorption in the visible light region, which improves the photoquantum efficiency of the composite photocatalyst in the visible light region and the degradation rate of photocatalytic MB. The higher specific surface area of the NTGB3 composite can absorb more light
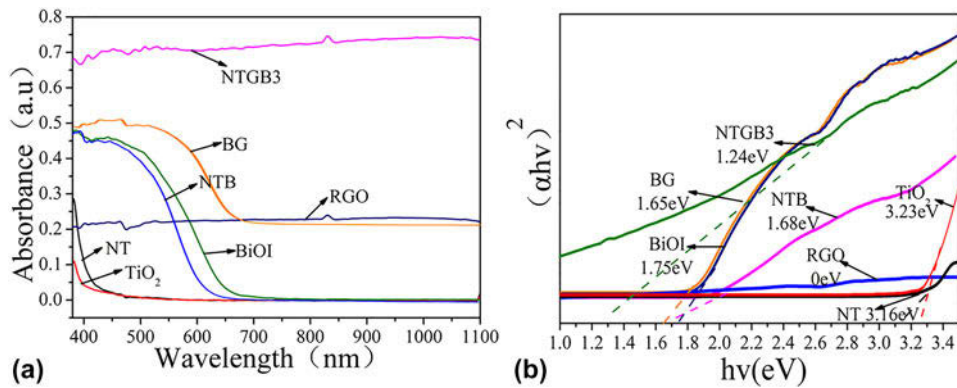
Figure 5: (a) UV-vis diffuse reflectance spectra of samples, (b) plots of $(a h\nu)^{1/2}$ versus photo energy ($h\nu$) of samples.
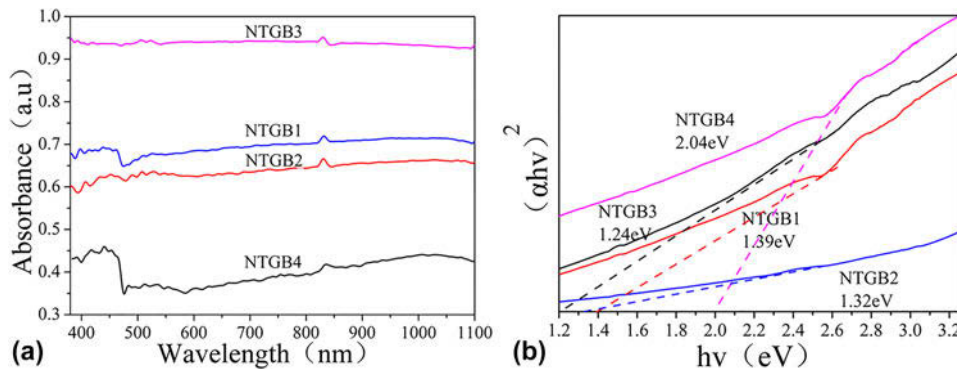

Figure 6: (a) UV-vis diffuse reflectance spectra of samples, (b) plots of $(a h\nu)^{1/2}$ versus photo energy ($h\nu$) of samples.
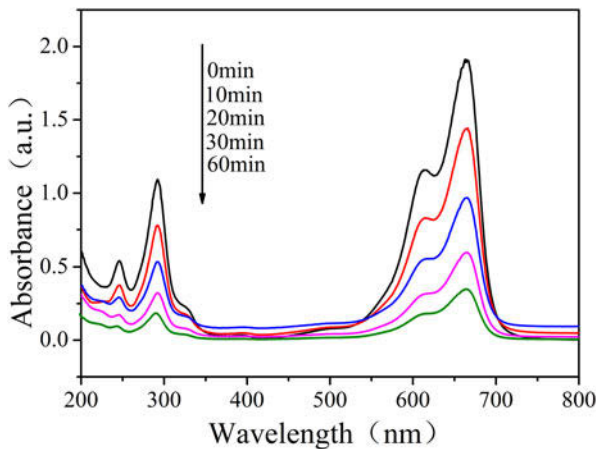

Figure 7: Absorption spectra of MB photocatalysts degraded by NTGB3 for different times.

intensity and generate more excitons, which is beneficial for the degradation of MB in the photocatalytic process.

Photocatalytic degradation of low-concentration organic pollutants is a multiphase surface reaction process, and its kinetics can be described by the Langmuir–Hinshelwood (L–H) model in the first-order simplified form $\ln(C/C_0) = k_1 t$ (where C is the concentration of organic pollutants, k_1 is the

first-order kinetic constant, and t is the reaction time). $\ln (C/C_0)$ plot versus t (since the concentration of the sample is basically unchanged after 30 min, so t is 0–30 min) affords a straight line with a slope of k_1. Figure 9 shows the first-order kinetic curves of degradation of MB by different catalysts. It can be seen that the first-order kinetic curves of degradation of MB by all samples are approximately a straight line. Moreover, the amount of RGO significantly affects the photocatalytic activity of the NTGB sample. They are 3.42, 3.25, 3.15, 2.98, 2.33, 1.82, 1.51, and 1.29 times for TiO_2 (0.0313 min^{-1}), NT (0.033 min^{-1}), BiOI (0.034 min^{-1}), NTB (0.036 min^{-1}), BG (0.046 min^{-1}), NTGB1 (0.083 min^{-1}), NTGB2 (0.071 min^{-1}), and NTGB4 (0.059 min^{-1}), respectively. RGO can play a role in enhancing the visible light absorption of composite photocatalysts.

Photocatalytic reaction mechanism

On the basis of the aforementioned information, a possible mechanism for MB photodegradation over the NTGB is proposed, as illustrated in Fig. 10. Photogenerated holes (h^+) and electrons (e^-) are generated in valence bands (VBs) and conduction bands (CBs) of NTGB composites, respectively. The photogenerated electrons in NT CBs can be quickly transferred to RGO and bind to holes in BiOI VB, leaving
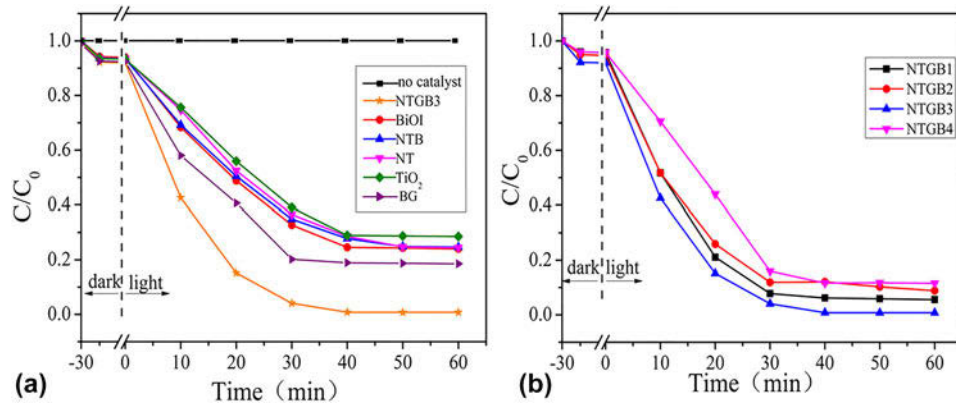
Figure 8: Photocatalytic degradation curves of MB loaded on (a) TiO_2, NT, NTB, BG, BiOI, and NTGB3 and (b) NTGB1, NTGB2, NTGB3, and NTGB4.
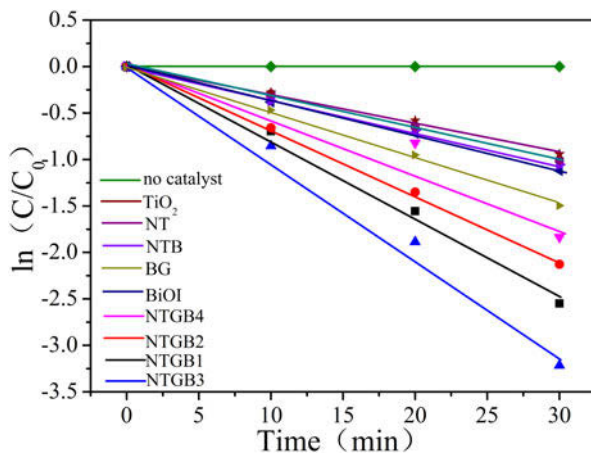

Figure 9: Kinetic curves of first-order reaction of MB degradation loaded on different catalysts.

Figure 10: Mechanism of MB degradation by NTGB.

electrons/holes in NT and BiOI for further reduction/oxidation reaction. Obviously, electrons on the CBs of BiOI with stronger reductive ability can drive the production of superoxide radical anions ($\bullet O^{2-}$) by reducing the amount of O_2 adsorbed on its surface, while H^+ on VBs with higher oxidation potential can produce more reactive $\bullet OH$ radicals for MB photodegradation. RGO with an off-domain conjugation structure and excellent conductivity can effectively act as an electron acceptor to suppress the fast charge-carrier recombination. In addition, RGO can increase both the absorption of incident light and the adsorption of organic pollutants on photocatalysts, thus significantly improving the degradation rate of MB.

Conclusion

A NTGB composite photocatalyst with visible light catalytic activity was prepared using a hydrothermal method. The results indicated that when the N-doped TiO_2 (Ti:N molar ratio of 1:1)/BiOI/RGO mass ratio is 1:1:2 (NTGB3), the prepared NTGB has a larger specific surface area, smaller
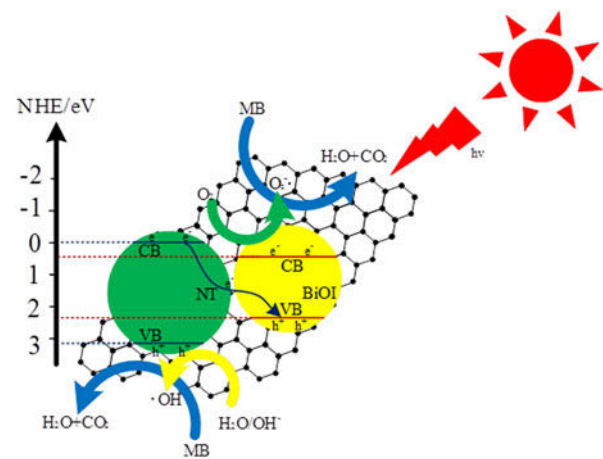
bandgap, and stronger absorption in the visible light region, and the degradation of MB under visible light has the best photocatalytic performance. The degradation rate of MB by NTGB is obviously higher than degradation by TiO_2, NT [30], BiOI, and NTB. The results demonstrate that NTGB photocatalysts are promising composite photocatalysts for the degradation of organic pollutants.

Experimental

Materials and reagents

GO was purchased from Shenzhen Tuling Evolutionary Technology Co. (Shenzhen, China) and used for the nanocomposite preparation. Other reagents and solvents were all purchased from Tianjin Chemical Reagent Co. (Tianjin, China). Solutions were prepared with deionized water.

Preparation of photocatalysts

TiO_2 was synthesized using a hydrothermal method. Complete mixing of 8 mL tetrabutyl titanate [$Ti(OBu)_4$] and 40 mL

absolute ethanol afforded solution A. Solution B (pH = 2–3) was prepared by adding 1.5 mL (36–38%) hydrochloric acid and 3.0 mL deionized water to 40 mL ethanol. Then, solution B was dropwise added into solution A. After that, the mixture was stirred for 30 min at room temperature, followed by stirring at 180 °C for 24 h. Then, the reaction mixture was removed from heat and stirred to allow the precipitation of the TiO_2 composite. The precipitate was filtered and washed with absolute ethanol and deionized water three times and then dried at 80 °C for 10 h to give a white powder. Finally, the powder was sintered at 450 °C for 3 h in a muffle furnace.

The preparation method of NT was consistent with TiO_2, except that urea was added in solution B to make the mole ratio of nTi in mixture A and B:nN = 1:1.

BiOI was synthesized using a hydrothermal method. First, 0.44 g $Bi(NO_3)_3 5H_2O$ and 0.15 g KI powder were successively added to deionized water. The pH of the solution was fixed at 8. Then, the mixture was transferred into an autoclave and treated at 180 °C for 24 h in a furnace. After cooling to room temperature, the reaction mixture was washed three times and then filtered. The residue was dried in an oven at 80 °C to afford BiOI.

NTB was synthesized using a hydrothermal method. Here, 10 mg NT was dispersed in 60 mL distilled water and ultrasonicated for 5 h. Then, 0.44 g $Bi(NO_3)_3 5H_2O$ and 0.15 g KI powder were successively added to the above solution under vigorous stirring. The pH of the solution was fixed at 8. Then, the mixture was transferred into an autoclave and treated at 180 °C for 24 h in a furnace. After cooling to room temperature, the reaction mixture was washed three times and filtered. The residue was dried in an oven at 80 °C to afford NTB.

BG was synthesized using a hydrothermal method. Here, 0.2 g of $Bi(NO_3)_3·5H_2O$ was added to the GO dispersed solution and stirred for 10 min. Then, 0.06 g of KI was stepwise added to the solution under stirring for 30 min and the reaction mixture was transferred into an autoclave and treated at 180 °C for 24 h in a furnace. The residue was dried in an oven at 80 °C to afford BG.

NTBG was synthesized using a hydrothermal method. Here, 0.2 g of NT powder was added to the GO dispersed solution and sonicated for 8 h. Further, 0.2 g of $Bi(NO_3)_3·5H_2O$ was added to the above solution and stirred for 10 min. Then, 0.06 g of KI was stepwise added under stirring for 30 min and the reaction mixture was transferred into an autoclave and treated at 180 °C for 24 h in a furnace. The hydrothermal reaction of GO at 180 °C afforded RGO [31]. After cooling to room temperature, the reaction mixture was washed three times and filtered. The residue was dried in an oven at 80 °C to afford the final NTGB composite. According to the different mass ratios of NT, BiOI, and RGO, the obtained products were defined as NTGB1 (1:1:1), NTGB2 (1:2:1), NTGB3 (1:1:2), and NTGB4 (2:1:1).

Characterization

The XRD patterns of the as-prepared samples were obtained on a Bruker 8-Advance diffractometer (Cu K$_\alpha$ = 0.15406 nm) at 40 kV. The 2θ ranged from 10° to 80° at a scan rate of 5°/min. XPS measurements were carried out on an Escalab-250Xi X-ray photoelectron spectrometer microprobe with an Al K$_\alpha$ source (150 W). The optical properties of the photocatalysts were estimated using a UV-vis spectrometer (Analytikjena, Germany) in the range from 200 to 800 nm. The UV-vis diffuse reflectance spectra (UV-vis DRS) of the catalysts were determined by a Shimadzu UV-2550 spectrophotometer using $BaSO_4$ as reference. Fourier transform infrared (FTIR) spectroscopy (NiCOLETIS5) was used for the examination of the functional groups in the 4000–500 cm^{-1} wavenumber region. The morphologies and composition of the samples were investigated using field emission scanning electron microscopy (FE-SEM; MX2600FE, U.K.). Nitrogen adsorption–desorption isotherms were obtained at 77 K on a V-SorbX800 surface area analyzer.

Photocatalytic evaluation

The photocatalytic activities of the as-prepared photocatalysts were evaluated by the degradation of MB (10 mg/L) under visible light irradiation (300 W Xenon lamp). In each test, 0.1 g photocatalyst was added into 100 mL of the MB aqueous solution with a certain concentration. Before irradiation, the suspension was stirred under dark condition for 30 min to establish an adsorption–desorption equilibrium between the MB molecules and photocatalysts. Then, 2 mL of the suspension was taken out for analysis at an interval of 10 min during each photocatalytic test. Concentration of the MB solutions was quantified using the Analytikjena spectrophotometer at 292 and 664 nm based on the absorbance change.

References

1. **H. Zhang, J.L. Zhang, and R.J. Sun**: Preparation of magnetic and photocatalytic cenosphere deposited with Fe_3O_4/SiO_2/Eu-doped TiO_2 core/shell nanoparticles. *J. Mater. Res.* **23**, 3700 (2015).
2. **S.R. Fu, Y.M. He, and Q. Wu**: Visible-light responsive plasmonic $Ag_2O/Ag/g$-C_3N_4 nanosheets with enhanced photocatalytic degradation of Rhodamine B. *J. Mater. Res.* **31**, 2252 (2016).

3. W. Zhang, C. Wang, and X. Liu: Enhanced photocatalytic activity in porphyrin-sensitized TiO_2 nanorods. *J. Mater. Res.* **23**, 1 (2017).

4. Y. Yan, T.R. Chen, and Y.C. Zou: Biotemplated synthesis of Au loaded Sn-doped TiO_2 hierarchical nanorods using nanocrystalline cellulose and their applications in photocatalysis. *J. Mater. Res.* **5**, 1383 (2016).

5. S. Chabri, A. Dhara, and B. Show: Mesoporous CuO–ZnO p–n heterojunction based nanocomposites with high specific surface area for enhanced photocatalysis and electrochemical sensing. *Catal. Sci. Technol.* **6**, 3238 (2016).

6. E.J. Park, H.J. Jo, H.J. Kim, K. Cho, and J. Jung: Effects of gamma-ray treatment on wastewater toxicity from a rubber products factory. *Radioanal. Nucl. Chem.* **277**, 619 (2008).

7. Z. Zheng, X.H. Zheng, H.T. Wang, and Q.G. Du: Macroporous graphene oxide-polymer composite prepared through pickering high internal phase emulsions. *ACS Appl. Mater. Interfaces* **5**, 7974 (2013).

8. X. Gu, L. Li, Y. Wang, P. Dai, H. Wang, and X. Zhao: Hierarchical tubular structures constructed from rutile TiO_2 nanorods with superior sodium storage properties. *Electrochim. Acta* **211**, 77 (2016).

9. X. Wang, Q. Meng, Y. Wang, H. Liang, Z. Bai, K. Wang, X. Lou, B. Cai, and L. Yang: TiO_2 hierarchical hollow microspheres with different size for application as anodes in high-performance lithium storage. *Appl. Energy* **175**, 488 (2016).

10. H. Irie, Y. Watanabe, and K. Hashimoto: Preparation, characterization and photocatalytic activity of composite catalyst $K_3PW_{12}O_{40}/TiO_2$. *Phys. Chem. B* **107**, 5483 (2005).

11. M. Batzill, E.H. Morales, and U. Diebold: First-principles study on electronic structure and optical properties of Ce-doped ZnO, CeN-co-doped TiO_2 and transparent conductive oxide $In_4Sn_3O_{12}$ and $In_4Ge_3O_{12}$. *Phys. Rev. Lett.* **96**, 026103 (2006).

12. D.V. Cristiana, P. Gianfranco, and S. Annabella: The energy band structure of S-TiO_2 was studied by first-principles method. *Phys. Chem.* **109**, 11414 (2005).

13. D.V. Cristiana, P. Gianfranco, and S. Annabella: Preparation characterization and photocatalytic properties of titanium dioxide doped with metal ions and metal ions. *Chem. Mater.* **17**, 6656 (2005).

14. Z.M. Wang, Y.M. Li, and R.H. Liao: Preparation and photocatalytic properties of NiO/TiO_2 nanotubes by hydrothermal method. *Acta Photonica Sin.* **48**, 031603 (2016).

15. H.J. Yang, M.Z. Shao, and J.X. Zhou: Study on photocatalytic activity and light corrosion resistance of Ag_2O/TiO_2 heterostructure. *J. Synth. Cryst.* **46**, 243 (2017).

16. C. Liu, Y. Yang, and W. Li: A novel Bi_2S_3 nanowire@TiO_2 nanorod heterogeneous nanostructure for photoelectrochemical hydrogen generation. *Chem. Eng. J.* **302**, 717 (2016).

17. X. Li, T. Xia, and C.H. Xu: Synthesis and photoactivity of nanostructured CdS–TiO_2 composite catalysts. *Catal. Today* **225**, 64 (2014).

18. S. Gao, C. Guo, and J. Lv: A novel 3D hollow magnetic Fe_3O_4/BiOI heterojunction with enhanced photocatalytic performance for bisphenol A degradation. *Chem. Eng. J.* **307**, 1055 (2017).

19. X. Li, J. Xia, and W. Zhu: Facile synthesis of few-layered MoS_2 modified BiOI with enhanced visible-light photocatalytic activity. *Colloid. Surf. Physicochem. Eng. Asp.* **511**, 1 (2016).

20. F.P. Huang, M.L. Cui, and Y.Y. Guo: Preparation and photocatalytic performance of TiO_2-BiOI with high visible activity. *Fine Chem. Eng.* **36**, 231 (2019).

21. C.X. Li, X. Yang, and G.W. Tan: Preparation and photocatalytic performance of WO_3/TiO_2–RGO composites. *J. Lanzhou Univ. Technol.* **43**, 25 (2017).

22. X. Lei, Y. Wei, and W. Guo: One-pot solvothermal preparation and enhanced photocatalytic activity of metallic silver and graphene co-doped $BiVO_4$ ternary systems. *Appl. Surf. Sci.* **332**, 682 (2015).

23. S. Shah: Single-step solvothermal syn-thesis of mesoporous Ag–TiO_2-reduced graphene oxide ternary composites with enhanced photocatalytic activity. *Nanoscale* **5**, 5093 (2013).

24. B.H. He, M.J. Zhou, and Z.H. Hou: Facile synthesis of Ni_3S_2/rGO nanosheets composite on nickel foam as efficient electrocatalyst for hydrogen evolution reaction in alkaline media. *J. Mater. Res.* **3**, 517 (2018).

25. Y.Y. Yu, M.Y. Yu, and Y. Zhang: Preparation and doping mechanism of nitrogen-doped titanium dioxide powders. *Chin. J. Inorg. Chem.* **29**, 1654 (2013).

26. L. Zhang, C.C. Zhao, and X.Y. Gao: Preparation of MoS_2/BiOI composite photocatalyst and its photocatalytic REDOX properties. *Acta Chim. Sin.* **11**, 1 (2018).

27. Z.K. Cui, F.L. Zhang, and Z. Zheng: In situ construction of BiOBr/Ag_3PO_4 composites with enhanced visible light photocatalytic performances. *J. Mater. Res.* **29**, 3254 (2014).

28. M. Thommes, K. Kaneko, and V. Neimark Alexander: Physisorption of gases, with special reference to the evaluation of surface area and pore size distribution (IUPAC technical report). *Pure Appl. Chem.* **64**, 1051 (2015).

29. A. Sharma and B.K. Lee: Integrated ternary nanocomposite of TiO_2/NiO/reduced graphene oxide as a visible light photocatalyst for efficient degradation of o-chlorophenol. *J. Environ. Manage.* **181**, 563 (2016).

30. F.J. Wu, X. Li, and W. Liu: Highly enhanced photocatalytic degradation of methylene blue over the indirect all-solid-state Z-scheme g-C_3N_4-RGO-TiO_2 nano heterojunctions. *Appl. Surf. Sci.* **405**, 60 (2017).

31. C. Burda, Y.B. Lou, and X.B. Chen: Enhanced nitrogen doping in TiO_2 nanoparticles. *Nano Lett.* **3**, 1049 (2003).